49th AIAA Aerospace Sciences Meeting including the New Horizons Forum and Aerospace Exposition
4 - 7 January 2011, Orlando, Florida

AIAA 2011-725

Low-Frequency Unsteadiness in DNS of Shock Wave/Turbulent Boundary Layer Interaction

Stephan Priebe*, M. Pino Martín†

The direct numerical simulation (DNS) of a compression ramp shock wave/ turbulent boundary layer interaction (STBLI) is presented. The ramp angle is 24°, and the inflow boundary layer conditions are Mach 2.9 and $Re_\theta = 2900$. For the discretization of the inviscid fluxes, a modified weighted essentially nonoscillatory (WENO) scheme is used. The numerical code has previously been validated in the context of a compression ramp DNS against experiments at matching flow conditions.[1,2] The low-frequency dynamics of the unsteadiness are investigated using low-pass filtered flow fields. It is observed that the nature of the shear layer changes depending on the phase of the shock motion, and it is conjectured that these changes are the manifestation of a shear layer instability.

I. Introduction

The interaction of a shock wave with a turbulent boundary layer (STBLI) is ubiquitous in compressible flow applications. Examples of flows involving such interactions are the flows over deflected control surfaces or inside super- and hypersonic engine inlets. A key feature of STBLIs is their strong unsteadiness. When the flow is separated, the shock is seen to oscillate in the streamwise direction at relatively low frequency. If U_∞/δ is the characteristic frequency of the energetic scales in the inflow boundary layer (here, U_∞ is the freestream velocity and δ is the 99% thickness of the boundary layer), then the characteristic frequency of the shock motion will typically be 1 to 2 orders of magnitude lower, i.e. $O(0.1 - 0.01U_\infty/\delta)$.[3,4]

The cause of the low-frequency unsteadiness is still under debate. It has been proposed that the shock motion is due to the upstream boundary layer, see e.g. Ganapathisubramani, Clemens and Dolling,[5] or, alternatively, that it is due to the downstream separated flow, see e.g. Dupont et al.,[6] Dussauge et al.,[7] Piponniau et al.[8] and Touber and Sandham.[9]

In this paper, we present the DNS of a 24° compression ramp at Mach 2.9 and Re_θ 2900. The analysis focuses on low-pass filtered flow fields and their evolution in time.

II. Numerical method and computational setup

The full three-dimensional unsteady Navier–Stokes equations in conservation form are solved for a perfect gas. The equations are expressed in dimensionless form and in a curvilinear coordinate system. The usual constitutive relations for a Newtonian fluid are used: the viscous stress tensor is linearly related to the rate of strain tensor, and the heat flux vector is linearly related to the gradient of temperature through Fourier's law of heat conduction. The coefficient of viscosity μ is computed from Sutherland's law, and the coefficient of thermal conductivity is computed from $k = \mu c_p/Pr$ where the molecular Prandtl number is taken to be 0.74. A detailed presentation of the governing equations may be found in Wu and Martín.[10]

The governing equations are solved using a fourth-order weighted essentially non-oscillatory (WENO) scheme to discretize the inviscid fluxes. Compared with the original finite-difference WENO scheme introduced by Jiang and Shu,[11] which is too dissipative for the accurate and efficient computation of STBLI flows, the present scheme is modified in two respects: the first modification concerns the linear part of the scheme, that is, the scheme as it is active in perfectly smooth flow regions where a set of optimal WENO weights is

*Graduate Student Member, Department of Mechanical and Aerospace Engineering, Princeton University. Visiting Graduate Student, Department of Aerospace Engineering, University of Maryland, College Park.
†AIAA Associate Fellow. Associate Professor, Department of Aerospace Engineering, University of Maryland, College Park.

engaged. The modification conists in adding a fully-downwinded candidate stencil, which gives a symmetric collection of candidate stencils, and in optimizing the WENO weights to maximize bandwidth-resolving efficiency.[12] The resulting symmetric bandwidth-optimized WENO scheme is still too dissipative for the accurate and efficient simulation of STBLI flows.[10] To reduce numerical dissipation further, the adaptation of the scheme away from the optimal weights in the presence of discontinuities (the nonliner part of the scheme) is modified by means of limiters.[10,13] An absolute limiter on the WENO smoothness measurement and a relative limiter on the total variation are used together, and the expressions for the limiters and the threshold values are given in Wu and Martín,[10] equations (12) and (17). For the discretization of the inviscid fluxes, standard fourth-order central differences are used, and time integration is performed by means of a third-order low-storage Runge–Kutta method.[14] The DNS code has been validated in previous work for supersonic shock wave/turbulent boundary layer interactions. The DNS by Wu and Martín[10] of supersonic flow over a compression ramp shows good agreement with experiments at matching flow conditions (see also refs[15,16]).

In addition to the DNS code being identical in the present simulation and the previous compression ramp simulation,[10] the general computational setup (domain, grid, initial and boundary conditions) is also identical, except for differences in the treatment of the inflow boundary condition. In the previous simulation,[10] the inflow boundary condition was specified by the recycling-rescaling technique developed by Xu and Martín,[17] and the rescaling was performed as part of the principal simulation. In the present simulation, the recycling-rescaling technique by Xu and Martín[17] is still used but we choose to perform the rescaling as part of an auxiliary boundary layer computation. There is no particularly deep reasoning for detaching the rescaling from the principal simulation and performing an auxiliary simulation beyond the obvious possibility of reusing the inflow data for other STBLI simulations and the associated savings in computational cost. Figure 1 shows the general setup for the DNS in the present work. The auxiliary DNS is performed on a grid consisting of 410×160×112 points in the streamwise, spanwise and wall normal direction (total of approximately 7.3 million points). The grid points are uniformely spaced in the streamwise and spanwise direction, whereas they are clustered in the wall normal direction according to a hyperbolic sine transformation. The principal DNS is performed on a grid consisting of 1024×160×128 points in the streamwise, spanwise and wall normal direction (total of approximately 21 million points). The grid points are uniformely spaced in the spanwise direction, whereas they are clustered in the streamwise and wall normal direction according to a hyperbolic sine transformation. The clustering in the streamwise direction is centered at the location of the corner. Unless otherwise stated, the reference plane at which grid resolutions, inflow conditions etc. will be stated in this paper is the inflow plane of the principal DNS (equivalently, the recycling plane of the auxiliary DNS). At the reference plane, the grid resolution in wall units in the streamwise direction is $\Delta x^+ = 7.5$, which is also the maximum grid spacing in the streamwise direction across the domain. The minimum grid spacing in the streamwise direction occurs at the corner and equals $\Delta x^+_{corner} = 3.5$ (where the nondimenionalizing viscous length scale is still taken at the reference plane). In the wall normal direction at the reference plane, the first grid point above the wall is located at $\Delta z^+_1 = 0.2$. The uniform grid spacing in the spanwise direction is $\Delta y^+ = 4.3$.

The initial flow field for the auxiliary DNS is generated according to the method of Martín,[18] whereas for the principal DNS a flow field from the previous DNS[10] is used for initialization.

Except for the inflow, the same boundary conditions are used in the auxiliary and principal DNS. A no-slip isothermal boundary condition is specified at the wall with $T_w = 307$K, which is approximately equal to the adiabatic wall recovery temperature. A supersonic outflow boundary condition is specified at the lid and outlet of the computational domain, and in the spanwise direction periodicity is specified. As discussed above, the inflow boundary condition for the auxiliary DNS is prescribed by means of the recycling-rescaling method of Xu and Martín.[17] At every time step in the auxiliary DNS, the flow data on four spanwise-wall normal planes surrounding the recycling plane is saved. As shown in figure 1 the saved flow data is used to prescribe the inflow boundary condition for the principal DNS. The data is required on four planes since fourth-order methods are used for the discretization of the viscous and inviscid fluxes and hence boundary condition data must be specified at four grid points. At runtime for the principal DNS, the saved inflow data is interpolated linearly in time to the instants dictated by the time stepping in the principal DNS. In addition, the saved inflow data is linearly interpolated from the auxiliary DNS grid onto the principal DNS grid. The interpolation is only required in the streamwise (x) and wall normal (z) direction, but not in the spanwise (y) direction in which the two grids are identical.

With the reference location fixed at the inflow of the auxiliary DNS, the autocorrelation of the u-velocity

as a function of streamwise separation (not shown here) decays to zero half way through the rescaling box, and this is the criterion according to which the rescaling length is selected. This selection criterion is based on the Eulerian decorrelation distance of the eddies, and as such it only guarantees the absence of spurious correlation being introduced in the rescaling box from a Eulerian viewpoint. Spurious periodicity could still be present in the flow since the Lagrangian decorrelation time of the eddies as they are being convected by the mean velocity is significantly larger as discussed by Simens et al.[19] Essentially, large-scale eddies take a significantly longer time to decorrelate with themselves as they are being convected by the mean velocity than suggested by the length scale of the autocorrelation function. For incompressible flows, Simens et al[19] argue that a large eddy of size $O(\delta)$, with internal velocity $O(u_\tau)$ and convection velocity $O(U_\infty)$ will decorrelate with itself as it convects over a distance $O(U_\infty \delta/u_\tau)$. Extending this argument to compressible flows, the eddy decorrelation length scale is $O(\sqrt{\rho_\infty} U_\infty \delta/\sqrt{\rho_w} u_\tau)$ since the appropriate velocity scale for a large eddy is $O(\sqrt{\rho_w} u_\tau/\sqrt{\rho_\infty})$ according to Morkovin's hypothesis. To eliminate spurious periodicty in the flow, the recycling plane would need to be located sufficiently far downstream from the inflow plane to accomodate the Lagrangian eddy decorrelation length, implying for the present flow conditions a rescaling length of $O(30\delta)$. Using such large rescaling lengths would be rather costly, and for the present simulation we choose a more moderate value, which satisfies the Eulerian decorrelation criterion but not the Lagrangian criterion. Consequently, some forcing due to the rescaling is present in the DNS but we argue that this forcing is acceptable for the purpose of the present study in the sense that it is restricted to narrow frequency bands associated with the principal rescaling frequency and a few of its higher-order harmonics, and moreover these frequencies are $O(0.1 - 1 U_\infty/\delta)$ and hence have disjoint frequency support from the low-frequency shock unsteadiness.

Under the conditions considered here, the coupling between the recycling and inflow plane appears to be mildly unstable in the free-stream, where a gradual increase of the turbulence level is observed over time, whereas inside the boundary layer the turbulence intensities are stationary. These observations hold over time scales corresponding to the duration of the DNS which is more than $1000\delta/U_\infty$. Instantaneous flow fields (not shown here) reveal that in the free-stream the forcing generates acoustic disturbances, which tend to be oriented in the vertical direction, originate some distance above the boundary layer at random locations in the free-stream and which can extend over large distances in the wall-normal and spanwise direction in some cases of the order of a few boundary layer thicknesses. There also appears to be a preference for acoustic waves travelling upstream with respect to the flow rather than downstream. This spurious free-stream mode is rather weak and only mildly unstable, raising the free-stream turbulence level to $O(0.1)$ over the entire duration of the DNS of $1000\delta/U_\infty$. Nevertheless, the quality of the simulation would be somewhat deteriorated by this spurious free-stream mode, and a modification is made in the auxiliary DNS with the purpose of damping this mode. The modification consists in periodically applying a free-stream filter in the auxiliary DNS. We consider this modification to be minor and non-intrusive in the sense that the filtering only acts in the free-stream and has no direct effect on the actual boundary layer flow. Details of this approach, including a validation of the auxiliary DNS demonstrating the accuracy of the free-stream filtering approach, may be found in Priebe and Martín.[20]

For completeness, it should be noted that a cartesian version of the DNS code is used in the auxiliary simulation (as opposed to the full curvilinar version used in the principal simulation). In addition, the WENO limiters are switched off in the auxiliary simulation, where the symmetric bandwidth-optimized WENO scheme is used on its own. The justification for this is that simulations of boundary layers are less stringent and may accurately be performed with the symmetric bandwidth-optimized WENO scheme on its own without the limiters.

III. Low-pass filtered flow fields

To investigate the unsteadiness, low-pass filtered flow fields and their evolution in time are presented in this section.

Data from two additional DNS runs is used in this section, and these are referred to as detailed simulation 1 and 2. They are identical to the simulation described thus far in terms of numerical method, computational setup and flow conditions, but the sampling frequency f_s at which the instantaneous three-dimensional flow field is output from the DNS is higher in the detailed simulations than in the original simulation: the sampling frequency is approximately $f_s\delta/U_\infty = 1$ in the original simulation, whereas it is approximately $f_s\delta/U_\infty = 10$ in the detailed simulations. This higher sampling frequency is necessary to obtain the time-resolved evolution

of the flow field. Both detailed simulations are started from a flow field from the original simulation, and both are run for approximately $200\delta/U_\infty$ (i.e. one fifth of the duration of the original simulation).

The motion of the low-pass filtered separation point $\tilde{x}_s$ during simulation 1 is shown in figure 2. A finite-impulse-response (FIR) filter with cutoff Strouhal number 0.22 has been used for low-pass filtering. The order of the filter is 300 (samples) meaning that its duration in the time domain is approximately $30\delta/U_\infty$. At the start of the data record in figure 2, the low-pass filtered separation point is located at approximately $\tilde{x}_s/\delta = -2.3$ and moves upstream ($d\tilde{x}_s/dt < 0$) at fairly constant speed. At $tU_\infty/L_{sep} = 45.5$, the separation point attains the most upstream location of the data record ($\tilde{x}_s/\delta = -2.55$), and subsequently it begins to move downstream ($d\tilde{x}_s/dt > 0$) at rapidly increasing speed. The maximum downstream-moving speed is attained near $tU_\infty/L_{sep} = 51$ and is significantly larger than the upstream-moving speed observed for $tU_\infty/L_{sep} < 45.5$. Following its rapid downstream motion, the separation point shows signs of stabilizing at a downstream location near $\tilde{x}_s/\delta = -1.95$ at approximately $tU_\infty/L_{sep} = 54$, only to move a short distance further downstream starting at $tU_\infty/L_{sep} = 58$. At $tU_\infty/L_{sep} = 60.5$, the separation point attains its most downstream location of $\tilde{x}_s/\delta = -1.85$, followed by a small upstream motion. The rest of the signal still shows some low-frequency oscillations but at smaller amplitude.

The first half of the separation point signal during simulation 1 may thus be described in summary as follows: a gradual upstream motion, followed by a rapid downstream motion and stabilization at a downstream location with subsequent mild upstream motion. The entire motion extends over a time of approximately $tU_\infty/L_{sep} = 35$. The evolution of the flow during this low-frequency motion may be seen from low-pass filtered fields. The starting point to obtain these fields is the time sequence of instantaneous three-dimensional flow fields sampled from the DNS. These are averaged in the spanwise direction, and the resulting fields in the (x, z)-plane are filtered in time. The filtering is performed at each grid point in the (x, z)-plane individually using the FIR filter described above.

Four low-pass filtered flow fields are shown in figure 3, and these fields correspond to the instants (a)-(d) indicated on the separation point signal in figure 2. In addition to the four key frames shown here, a movie of the entire time-resolved evolution of the low-pass filtered flow field will be presented during the talk. The low-pass filtered flow fields are plotted as follows: an isocontour of pressure gradient $|\nabla p|\delta/p_\infty = 2$ indicates the shock, (u, w)-streamlines indicate the state of the recirculating flow in the corner, and a color contour map of the spanwise vorticity indicates the structure of the region of shear above the recirculating flow. In addition, the u-velocity profile at $x/\delta = -4$ (shown as an inset) indicates the state of the inflow boundary layer.

In the first frame (figure 3(a)), the bubble is large and the shock is in an upstream location. The streamlines are fairly closely- and uniformly-spaced in the initial part of the separated shear layer ($-2 \leq x/\delta \leq -1$) and above the bubble with a band of strong vorticity/shear extending from the separation point downstream, making an angle with the wall and lying above the recirculation bubble. The movie reveals that at the instant corresponding to the first frame the bubble is growing and the shock is moving upstream, consistent with the observations made on figure 2. There is some indication that the structure of the separated shear layer is beginning to change around the time of the second frame (figure 3(b)). The movie shows that the shock attains its most upstream location at that time (consistent with the observations made on figure 2) and that in the initial part of the shear layer ($-2 \leq x/\delta \leq -1$), the streamline shown closest to the wall is pushed towards the wall as it diverges from its neighbor further away in the flow. Concurrently, a secondary region of high vorticity develops along the wall downstream of separation in addition to the main branch of strong vorticity in the flow, and the recirculation bubble begins to shrink. The divergence of the streamlines in the initial separated shear layer and the development of a secondary region of high vorticity along the wall are visible, in their initial stages, in figure 3(b). The third frame (figure 3(c)) is obtained around the time when the separation point is moving downstream at maximum speed (see the separation point signal in figure 2). The movie shows that the recirculation bubble is rapidly shrinking at this time and the shock is moving downstream. The changes in the structure of the shear layer that were hinted at in figure 3(b) are pronounced in figure 3(c): The region of strong vorticity downstream of separation is bifurcated with one branch in the flow, making an angle with the wall, and another branch along the wall. In the fourth frame (figure 3(d)), the shock is stabilized in a fairly downstream location, the bubble has recovered to some intermediate size, and the bifurcation of the shear layer has disappeared. It may be noted that the general structure of the flow in figures 3(a) and 3(d) is similar (although there are differences in bubble size and shock position).

A direct comparison of figure 3(a) (bubble growth phase) with figure 3(c) (bubble shrinking phase) shows

the different structure in the flow downstream of separation depending on the phase of the shock motion. Whereas the shock is in a fairly similar position in both figures, the structure of the flow downstream of separation is rather different (single branch of strong vorticity in the flow versus bifurcated structure with two branches of strong vorticity, the second branch being along the wall; large versus small bubble; closely- and uniformely-spaced streamlines downstream of separation versus diverging streamlines). To further qualify the low-frequency evolution of the shear layer, profiles of u-velocity and spanwise vorticity ω_y are plotted in figures 4-7, where the four figures correspond to the instants discussed thus far. The shear layer profiles in figure 4 generally resemble those of a plane mixing layer with a low-speed side near the wall and a high-speed side in the free-stream, connected by a profile that has one global inflection point. In figure 5, there is some indication of departures from this type of profile. At $x/\delta = -1.5$, the ω_y-profile (figure 5(c)) shows three extrema: a maximum near the wall, followed further above the wall by a minimum and yet further above the wall by another maximum. The u-velocity profile at the same location (figure 5(a)) shows a departure from the type of profile seen in figure 4(a) in the sense that it contains a high-velocity 'bulge' near the wall. Similar but more pronounced high-velocity 'bulges' are visible in all profiles from $x/\delta = -1.5$ to -0.5 in figure 6(a), and these profiles look distinctly different from those in figure 4(a). It appears that, in fact, the flow in figure 6 reattaches in a region downstream of separation and upstream of the corner. In the range $x/\delta = -1.5$ to -0.5, the vorticity profiles show large values close to the wall, followed some distance above the wall by a minimum and yet further above the wall by another maximum. The profiles in figure 7 have returned to the type of profile seen in figure 4 showing plane-mixing-layer-like behavior with a single global inflection point in the layer.

The observations made above about the low-frequency cycle in detailed simulation 1 are confirmed by detailed simulation 2. The motion of the separation point in detailed simulation 2 is shown in figure 8. The signal displays a series of upstream-downstream motions at a Strouhal number of approximately 0.1. While this frequency may be somewhat higher than the central frequency of the shock motion, it falls within the broadband peak surrounding the central frequency and it is disjoint of any other time scale in the flow (rescaling or turbulence), and the motion in figure 8 is thus attributable to the low-frequency unsteadiness.

Four low-pass filtered flow fields for detailed simulation 2 are shown in figure 9. In addition, a movie of the entire time-resolved evolution of the low-pass filtered flow field will be shown during the talk. Instants (a) and (c) are obtained as the separation point moves downstream ($d\tilde{x}_s/dt > 0$, see figure 8). At these instants, the low pass-filtered fields (figure 9(a) and (c)) show a bifurcated shear layer structure similar to that previously observed in figure 3(c). In addition, the movie shows that at the time of figure 9(a) and (c), the recirculation bubble is shrinking and the shock is moving downstream. Instants (b) and (d) are obtained as the separation point moves upstream ($d\tilde{x}_s/dt < 0$, see figure 8). The corresponding low-pass filtered flow fields (figure 9(b) and (d)) are similar to those previously discussed in figure 3(a) and (d). The recirculation bubble is fairly large, and the streamlines are fairly closely- and uniformly-spaced in the initial separated shear layer and above the bubble. A single branch of strong vorticity extends from separation downstream into the flow, making an angle with the wall and lying above the recirculation bubble. The movie shows that the bubble is growing and the shock is moving upstream at these instants.

The velocity- and vorticity-profiles for the four instants discussed are shown in figures 10-13. Figures 11 and 13 show shear layer velocity profiles that resemble those of a plane mixing layer, whereas the profiles in figures 10 and 12 show the previously discussed departures from this type of profile. In figure 10, the profiles have high-velocity 'bulges' near the wall for x/δ from -1.25 to -0.5, and in figure 12 these are visible for x/δ from -1.5 to -0.75.

IV. Low-frequency modulation of high-frequency shear layer structures

To investigate the possible low-frequency modulation of high-frequency energetic shear layer structures, we have perfomed another detailed simulation (detailed simulation 3). The motion of the separation point in this simulation is shown in figure 14. It appears that the intensities in the shear layer are strong when the shock is in an upstream location (figure 15(b) and (d)), whereas they are weak when the shock is in a downstream location (figure 15(a) and (c)).

V. Conclusions

Based on low-pass filtered flow fields, three main observations have been made above about the low-frequency unsteadiness, and these may be summarized as follows: (1) The motion of the shock and the pulsation of the bubble are related. The growth of the bubble is associated with the shock moving upstream, whereas the shrinking of the bubble is associated with the shock moving downstream. (2) The structure of the separated shear layer changes depending on the phase of the low-frequency motion. As the bubble grows, a single branch of strong vorticity exists downstream of separation, making an angle with the wall and lying above the recirculation bubble. The shear layer velocity profiles resemble those of a plane mixing layer with a single inflection point. As the bubble shrinks, the vorticity field downstream of separation has a bifurcation with a second branch of strong vorticity along the wall where the flow is reattaching. The shear layer velocity profiles contain a high-velocity 'bulge' near the wall and at least two inflection points, which distinguishes them from plane mixing layer profiles. (3) There is some indication that the intensity of the high-frequency energetic structures in the shear layer is modulated at low frequency.

We conjecture that the observed changes in the shear layer as a function of the phase of the shock motion are manifestations of an intrinsic shear layer instability and that this instability could be at the origin of the low-frequency unsteadiness.

Acknowledgments

This work was supported by the Air Force Office of Scientific Research under grant number AF 9550-09-1-0464. The authors would like to thank Yin-Chiu Kan for helping to prepare the movies.

References

[1]Wu, M. and Martin, M. P., "Direct Numerical Simulation of Supersonic Turbulent Boundary Layer over a Compression Ramp," *AIAA Journal*, Vol. 45, No. 4, 2007, pp. 879–889.

[2]Ringuette, M. J., Wu, M., and Martin, M. P., "Low Reynolds Number Effects in a Mach 3 Shock Turbulent Boundary Layer Interaction," *AIAA Journal*, Vol. 46, No. 7, 2008.

[3]Smits, A. J. and Dussauge, J. P., *Turbulent Shear Layers in Supersonic Flow*, Springer Verlag, New York, 2nd ed., 2006.

[4]Dolling, D., "Fifty Years of Shock-Wave/Boundary-Layer Interaction Research: What Next?" *AIAA Journal*, Vol. 39, No. 8, 2001, pp. 1517–1531.

[5]Ganapathisubramani, B., Clemens, N. T., and Dolling, D. S., "Effects of upstream boundary layer on the unsteadiness of shock-induced separation," *Journal of Fluid Mechanics*, Vol. 585, 2007, pp. 369–394.

[6]Dupont, P., Haddad, C., and Debiève, J. F., "Space and time organization in a shock-induced separated boundary layer," *Journal of Fluid Mechanics*, Vol. 559, 2006, pp. 255–277.

[7]Dussauge, J. P., Dupont, P., and Debiève, J. F., "Unsteadiness in Shock Wave Boundary Layer Interactions with Separation," *Aerospace Science and Technology*, Vol. 10, No. 2, 2006.

[8]Piponniau, S., Dussauge, J., Debiève, J., and Dupont, P., "A simple model for low-frequency unsteadiness in shock-induced separation," *Journal of Fluid Mechanics*, Vol. 629, 2009, pp. 87–108.

[9]Touber, E. and Sandham, N., "Large-eddy simulation of low-frequency unsteadiness in a turbulent shock-induced separation bubble," *Theoretical and Computational Fluid Dynamics*, Vol. 23, 2009, pp. 79–107.

[10]Wu, M. and Martín, M., "Direct numerical simulation of supersonic turbulent boundary layer over a compression ramp," *AIAA Journal*, Vol. 45, No. 4, 2007, pp. 879–889.

[11]Jiang, G.-S. and Shu, C.-W., "Efficient implementation of weighted ENO schemes," *Journal of Computational Physics*, Vol. 126, No. 1, 1996, pp. 202–228.

[12]Martín, M., Taylor, E., Wu, M., and Weirs, V., "A bandwidth-optimized WENO scheme for the effective direct numerical simulation of compressible turbulence," *Journal of Computational Physics*, Vol. 220, No. 1, 2006, pp. 270–289.

[13]Taylor, E., Wu, M., and Martín, M., "Optimization of nonlinear error for weighted essentially non-oscillatory methods in direct numerical simulations of compressible turbulence," *Journal of Computational Physics*, Vol. 223, No. 1, 2007, pp. 384–397.

[14]Williamson, J. H., "Low-storage Runge–Kutta schemes," *Journal of Computational Physics*, Vol. 35, No. 1, 1980, pp. 48 – 56.

[15]Ringuette, M., Wu, M., and Martín, M., "Low Reynolds number effects in a Mach 3 shock/turbulent-boundary-layer interaction," *AIAA Journal*, Vol. 46, No. 7, 2008, pp. 1884–1887.

[16]Ringuette, M., Bookey, P., Wyckham, C., and Smits, A., "Experimental study of a Mach 3 compression ramp interaction at $Re_\theta = 2400$," *AIAA Journal*, Vol. 47, No. 2, 2009, pp. 373–385.

[17]Xu, S. and Martín, M., "Assessment of inflow boundary conditions for compressible turbulent boundary layers," *Physics of Fluids*, Vol. 16, No. 7, 2004, pp. 2623–2639.

[18]Martín, M., "Direct numerical simulation of hypersonic turbulent boundary layers. Part 1. Initialization and comparison with experiments," *Journal of Fluid Mechanics*, Vol. 570, 2007, pp. 347–364.

[19]Simens, M., Jiménez, J., Hoyas, S., and Mizuno, Y., "A high-resolution code for turbulent boundary layers," *Journal of Computational Physics*, Vol. 228, No. 11, 2009, pp. 4218–4231.

[20]Priebe, S. and Martín, M., "Analysis of low-frequency unsteadiness in the direct numerical simulation of a shockwave and turbulent boundary layer interaction," *39th AIAA Fluid Dynamics Conference*, 2009, paper 2009-3711.

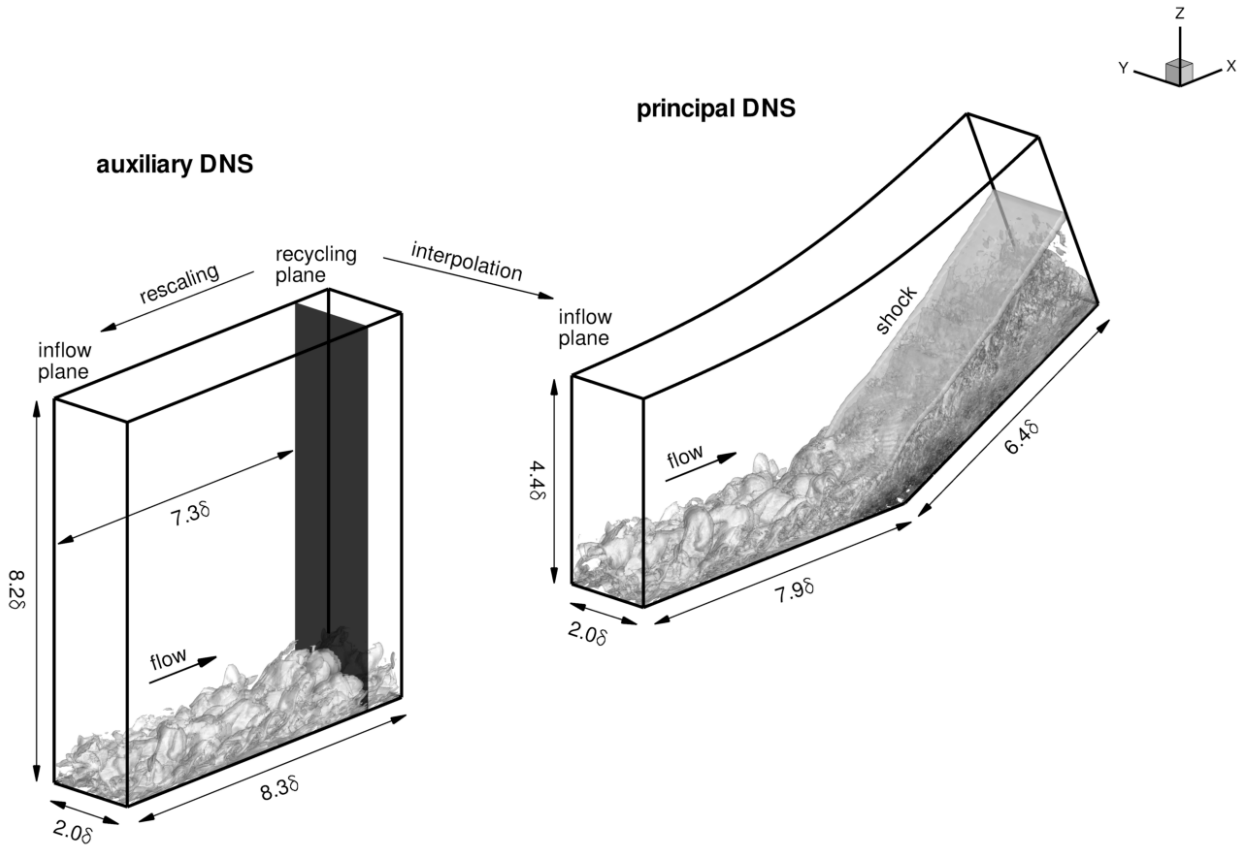

Figure 1. Computational domain and strategy for prescribing the inflow boundary condition. The reference length δ is the thickness of the boundary layer (based on 99% of the free-stream velocity) at the inflow plane of the principal DNS. An instantaneous flow field is shown in the domain, visualized by an isosurface of the magnitude of density gradient, $|\nabla\rho|\delta/\rho_\infty = 2.5$. The isosurface is colored by the streamwise velocity component (with levels from $-0.4U_\infty$ to U_∞, black to white). Note that x, y and z are, respectively, the streamwise, spanwise and wall normal coordinate.

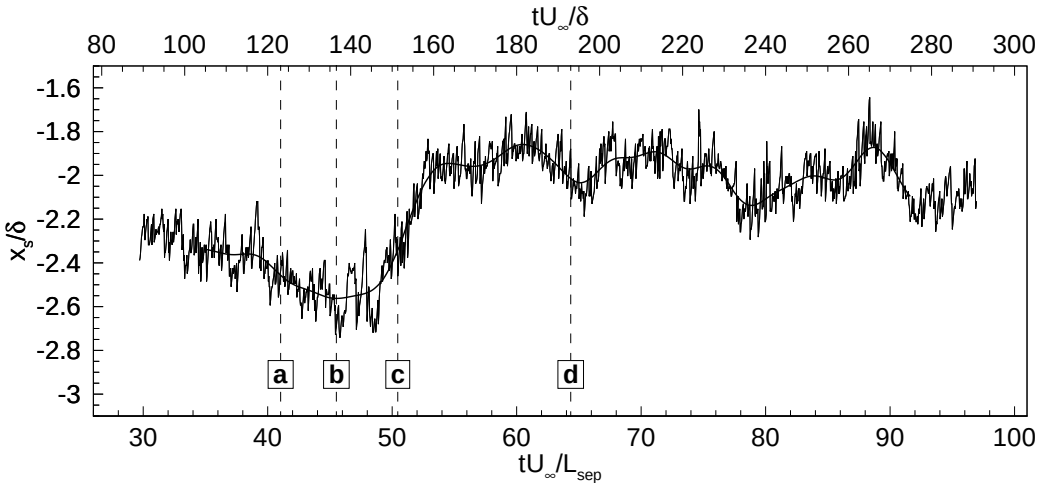

Figure 2. Location of spanwise-averaged separation point for detailed simulation 1. The low-pass filtered signal is also shown (cutoff Strouhal number 0.22). The vertical dashed lines with letters indicate the instants at which the flow fields in figures 3(a)-(d) are obtained.

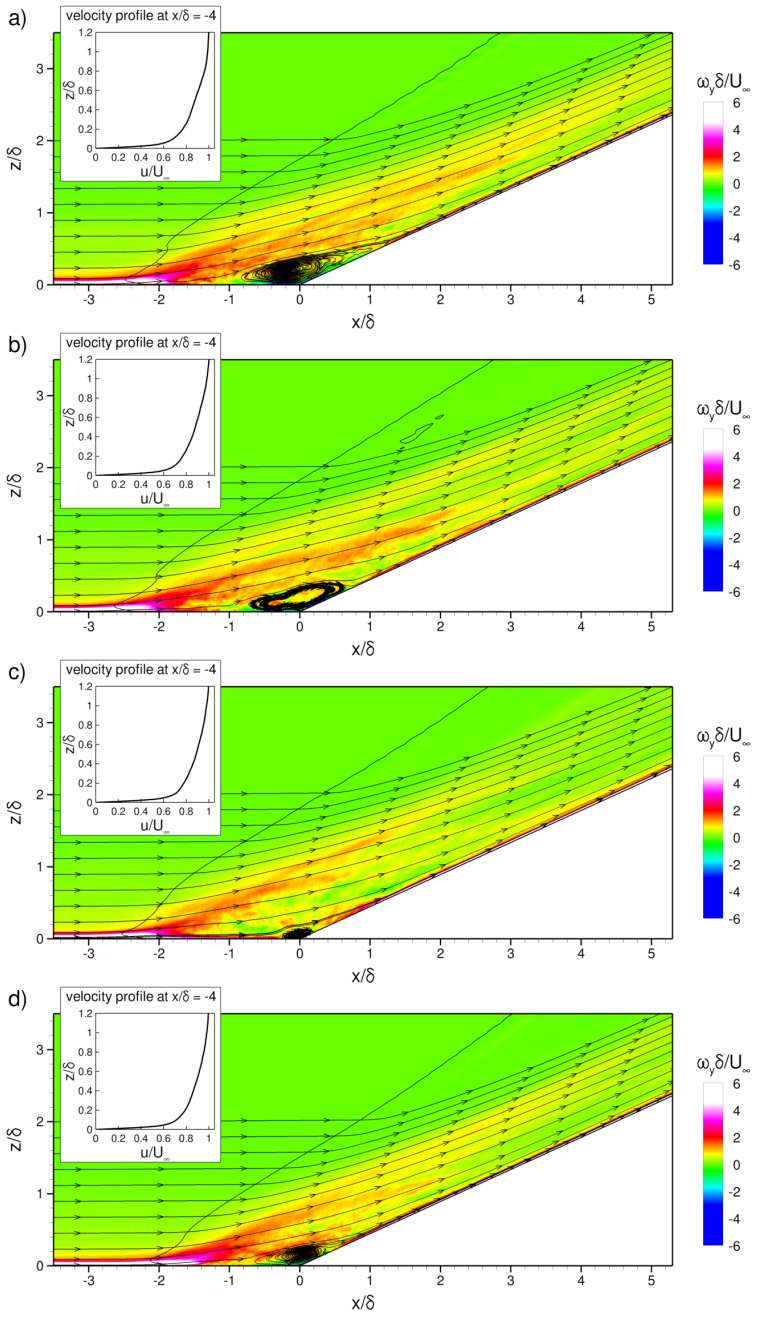

Figure 3. Spanwise-averaged low-pass filtered flow fields at the instants indicated in figure 2.

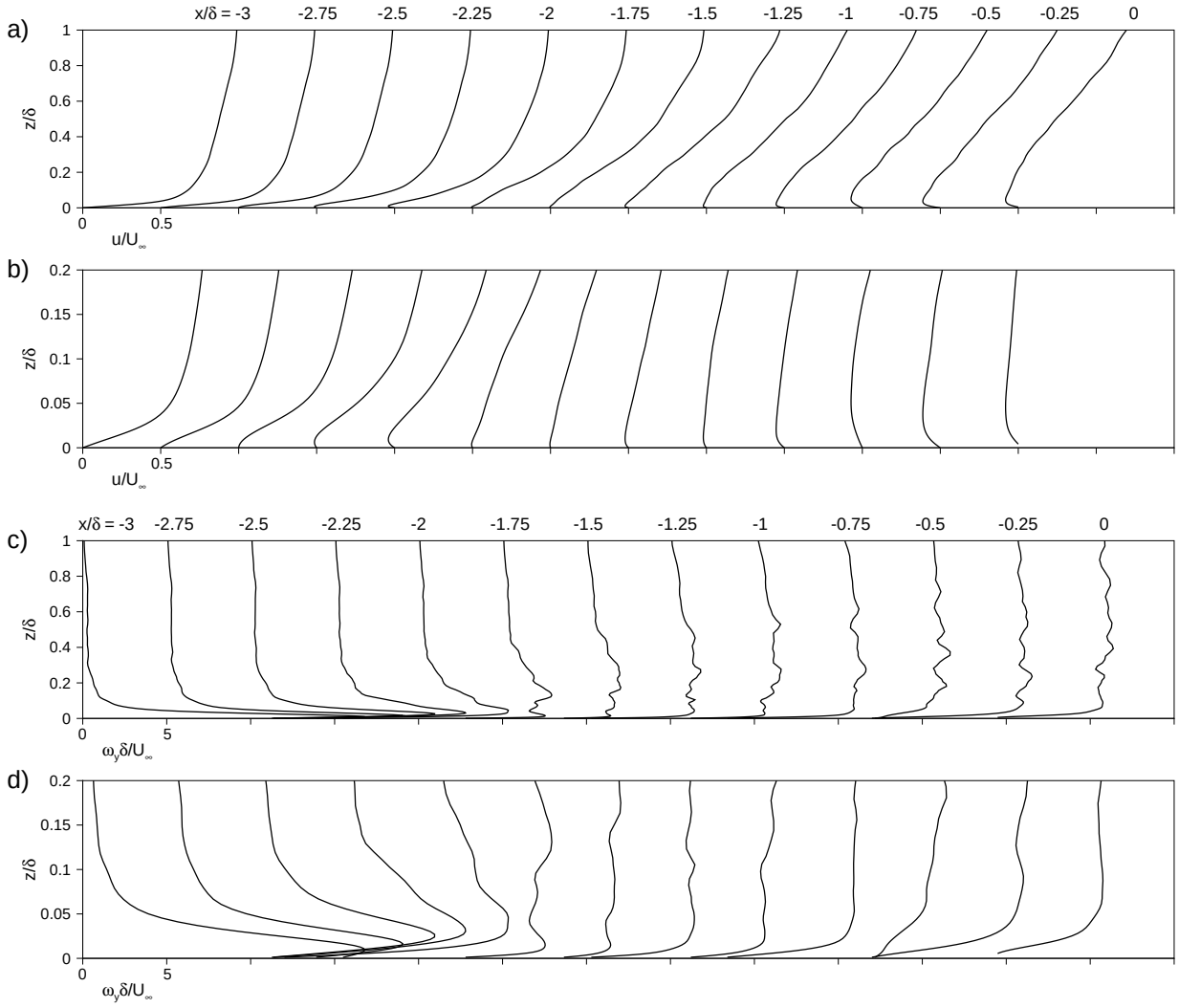

Figure 4. Profiles corresponding to the low-pass filtered flow field shown in figure 3(a). (a) streamwise velocity, (b) detail of streamwise velocity near wall, (c) spanwise vorticity, and (d) detail of spanwise vorticity near wall.

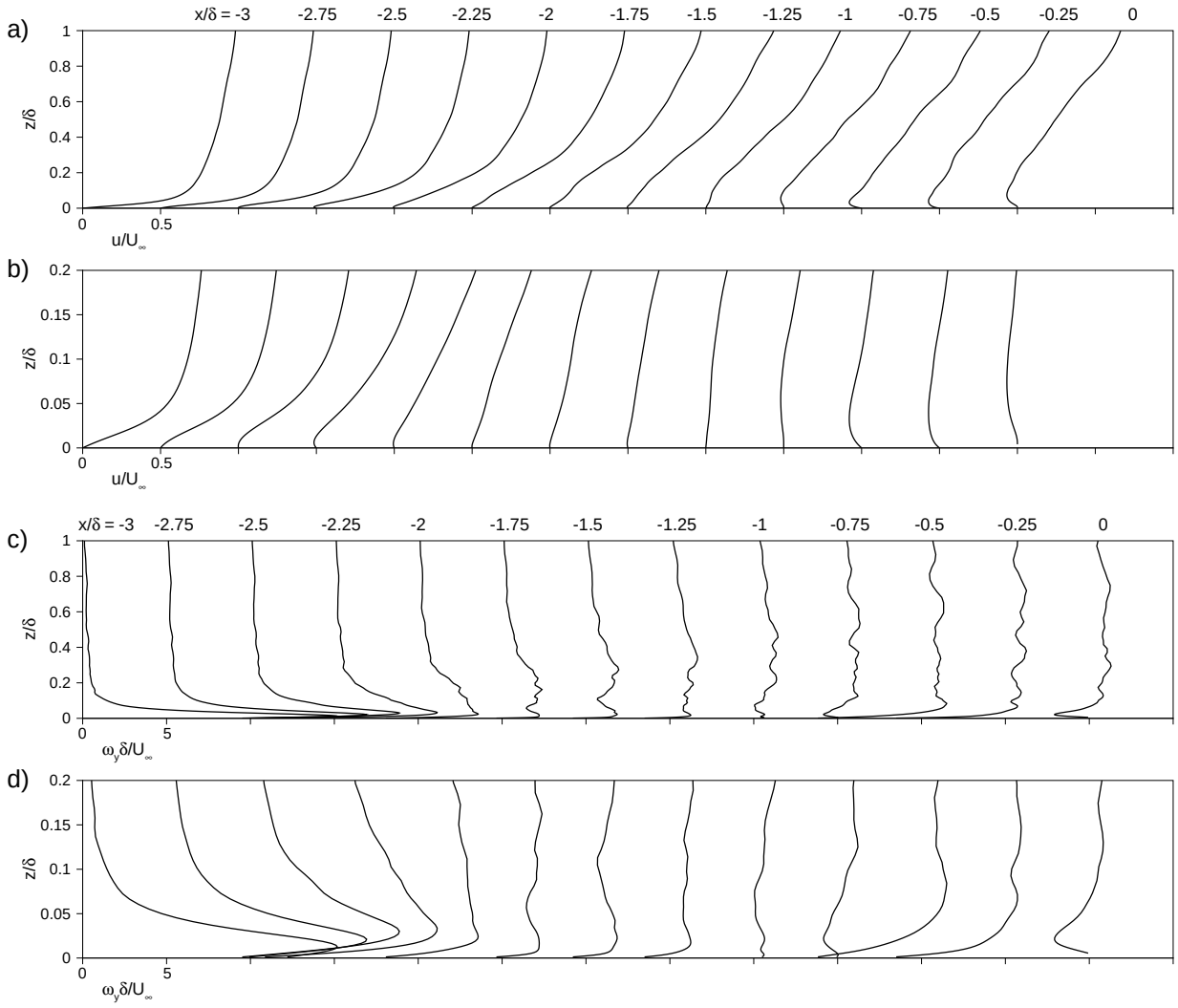

Figure 5. Same as figure 4, except that the profiles correspond to the low-pass filtered flow field shown in figure 3(*b*).

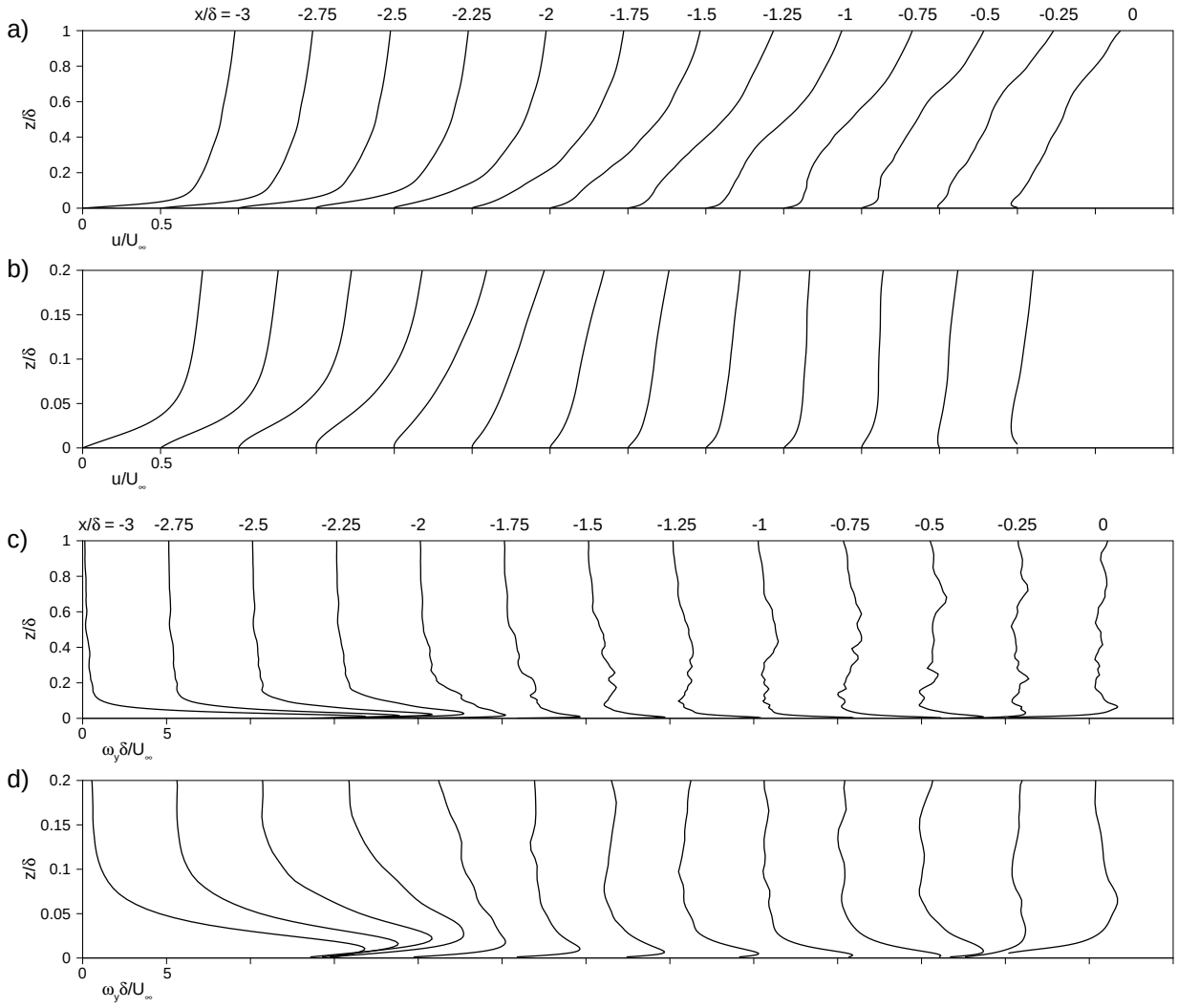

Figure 6. Same as figure 4, except that the profiles correspond to the low-pass filtered flow field shown in figure 3(*c*).

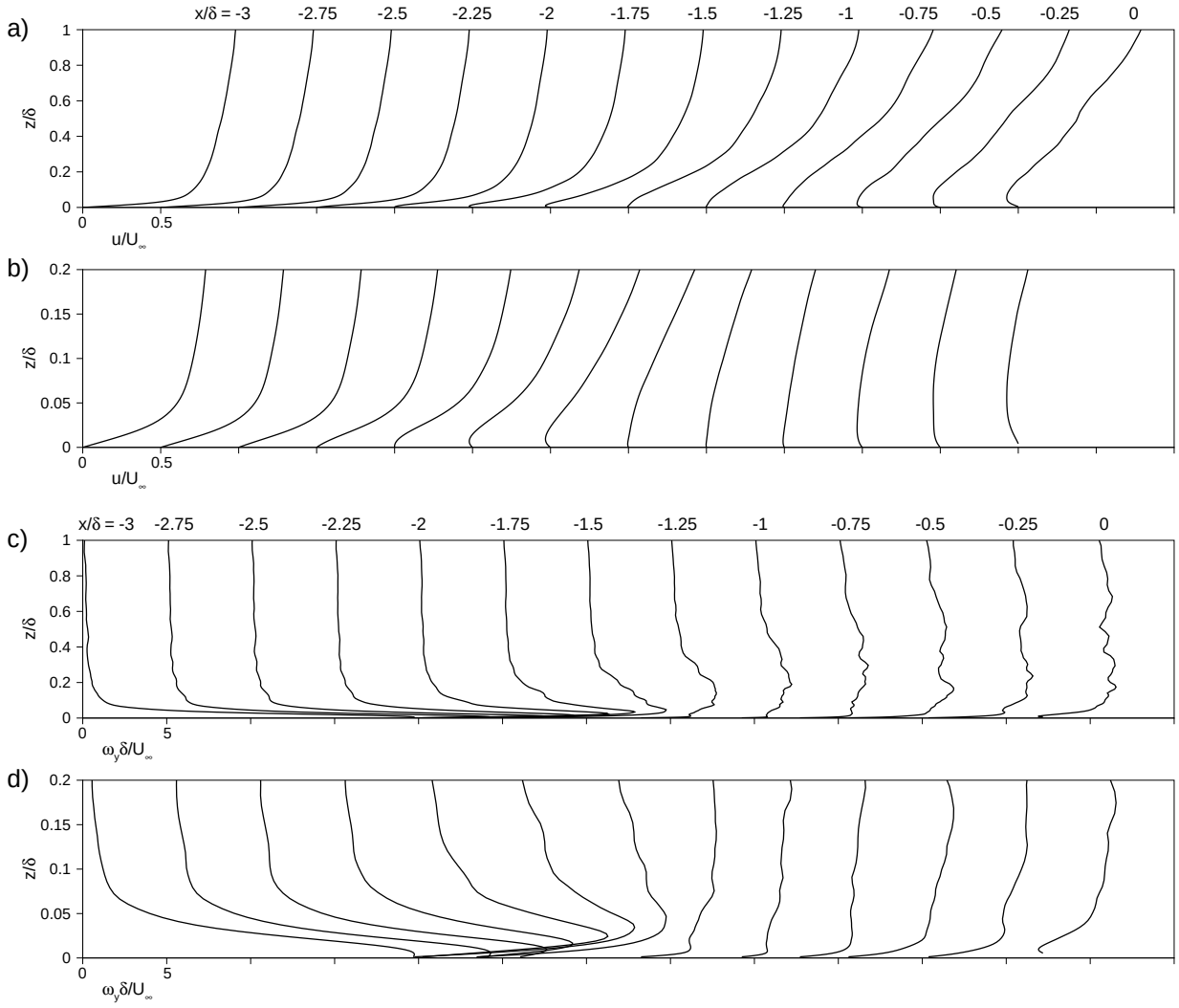

Figure 7. Same as figure 4, except that the profiles correspond to the low-pass filtered flow field shown in figure 3(d).

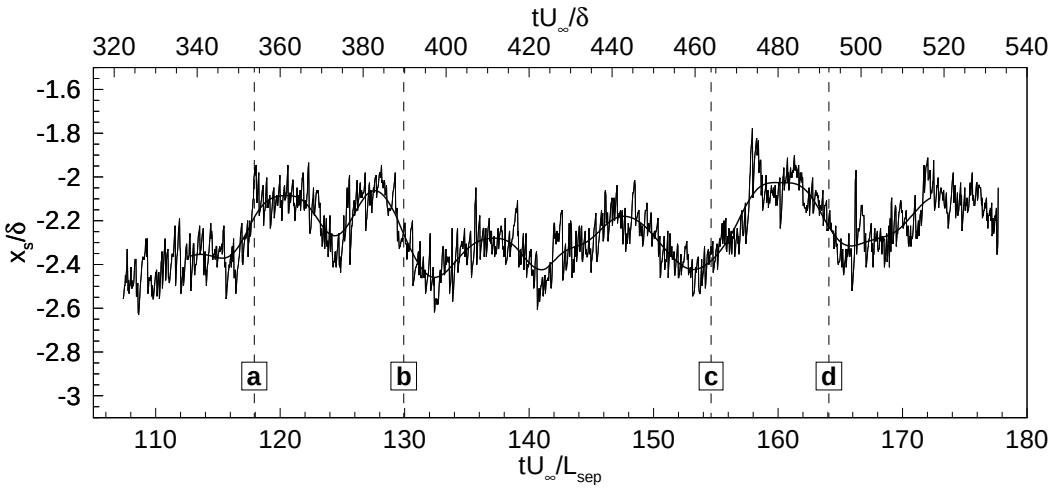

Figure 8. Location of the spanwise-averaged separation point for the detailed simulation 2. The low-pass filtered signal is also shown (cutoff Strouhal number 0.22). The vertical dashed lines with letters indicate the instants at which the flow fields in figures 9(a)-(d) are obtained.

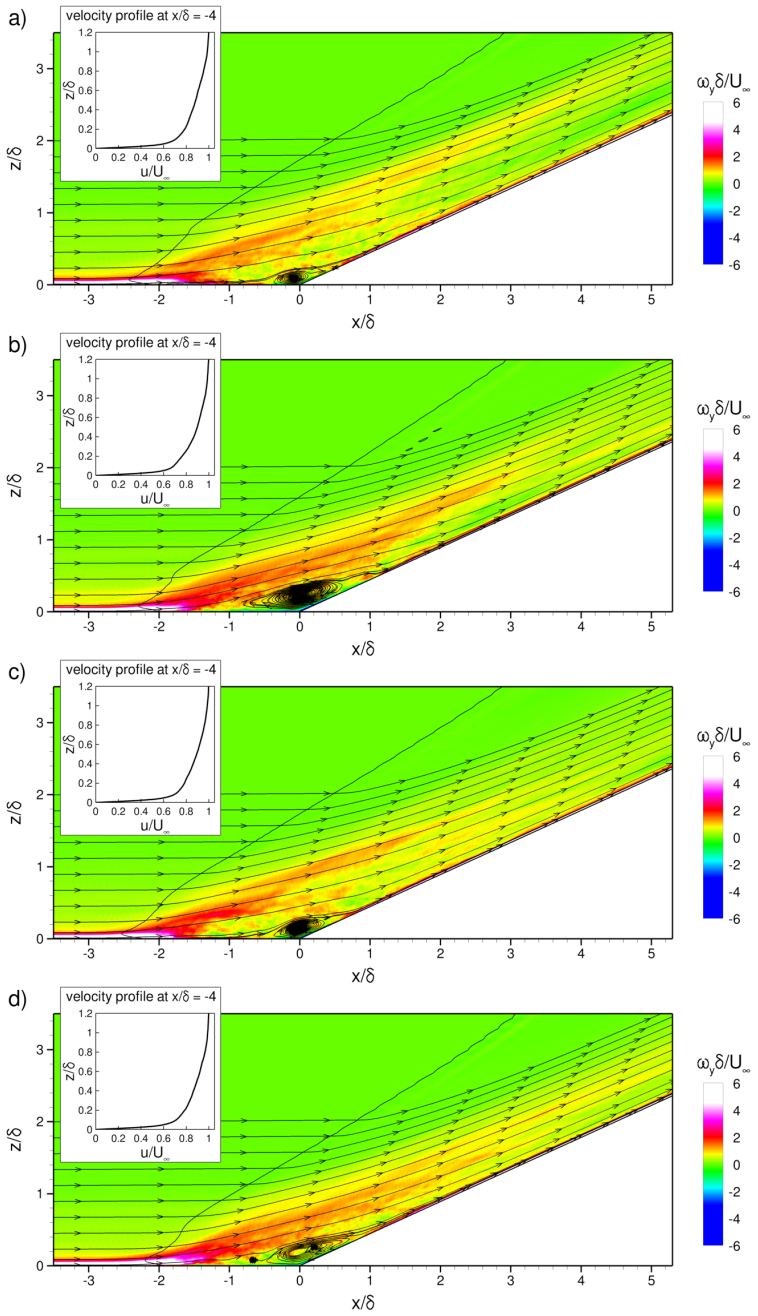

Figure 9. Spanwise-averaged low-pass filtered flow fields at the instants indicated in figure 8. See text for further details.

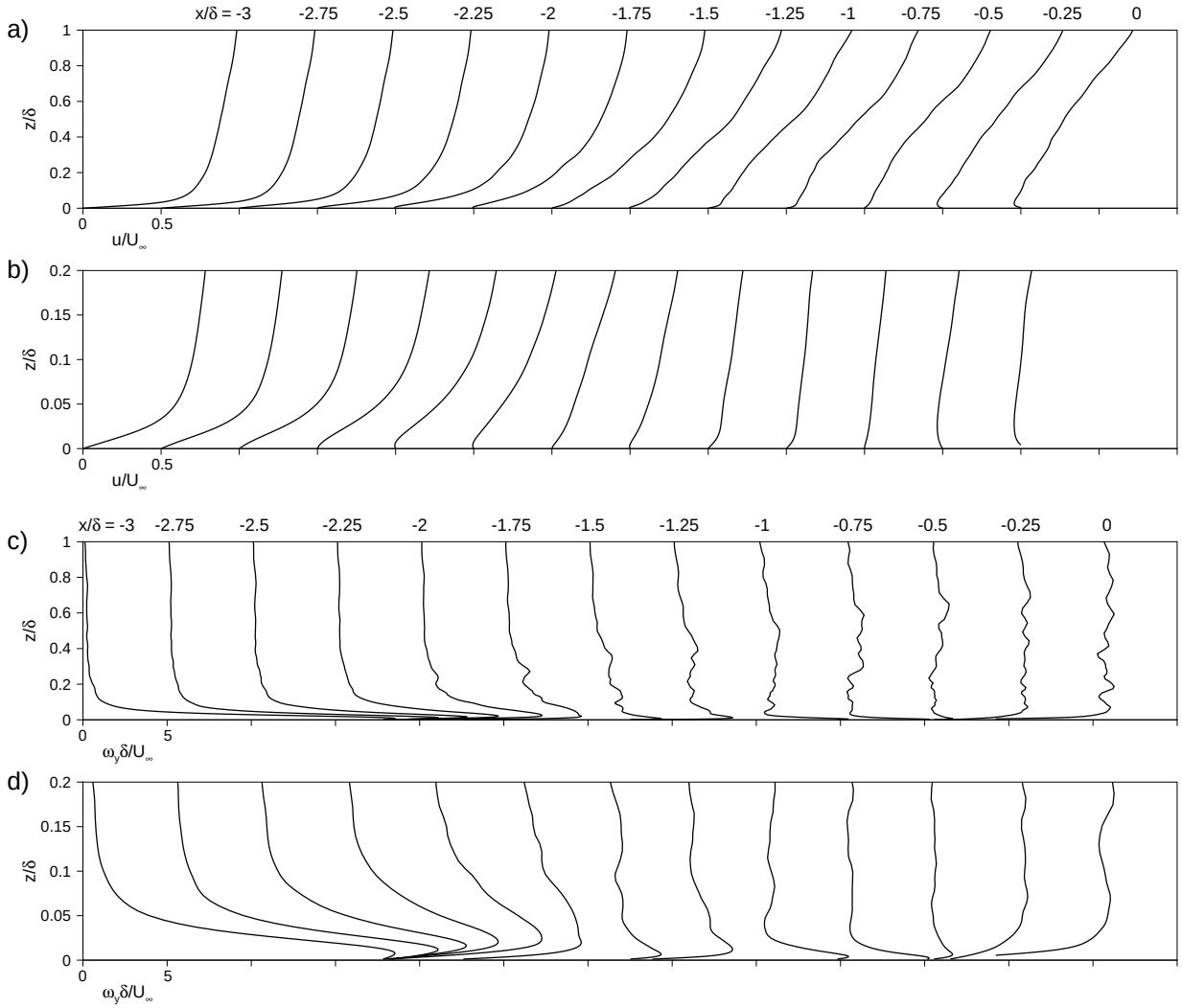

Figure 10. Profiles corresponding to the low-pass filtered flow field shown in figure 9(a). (a) streamwise velocity, (b) detail of streamwise velocity near wall, (c) spanwise vorticity, and (d) detail of spanwise vorticity near wall.

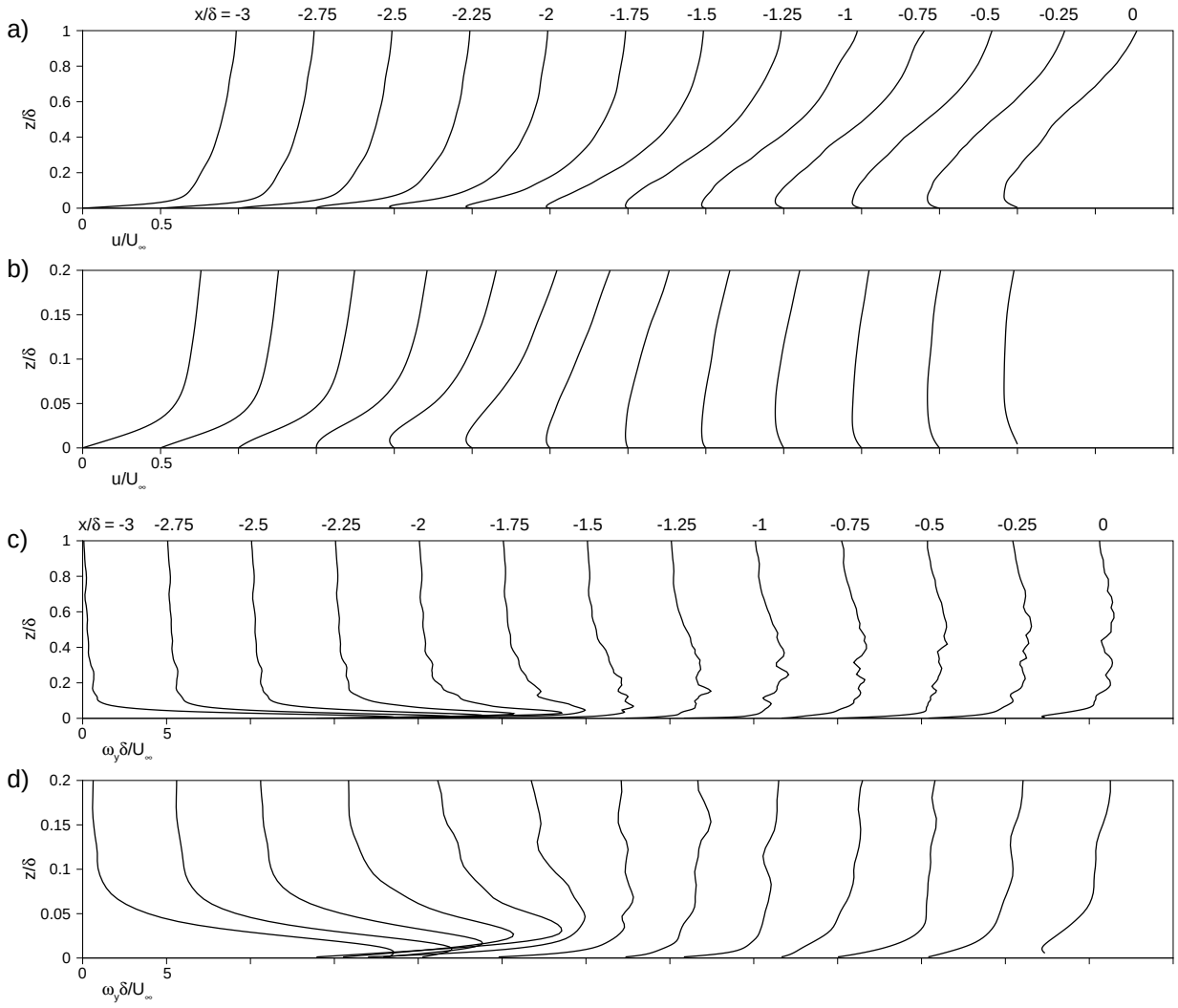

Figure 11. Same as figure 10, except that the profiles correspond to the low-pass filtered flow field shown in figure 9(b).

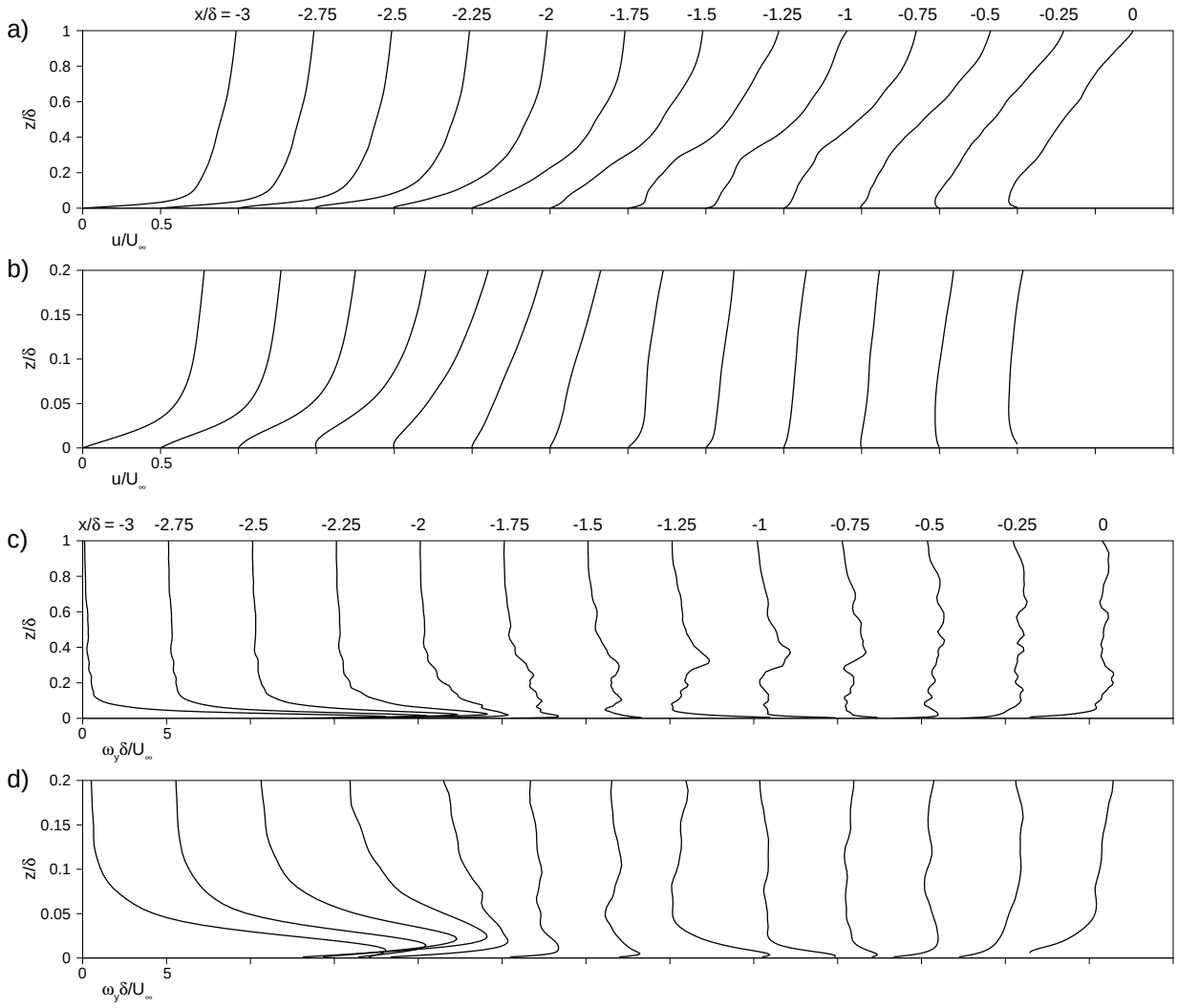

Figure 12. Same as figure 10, except that the profiles correspond to the low-pass filtered flow field shown in figure 9(*c*).

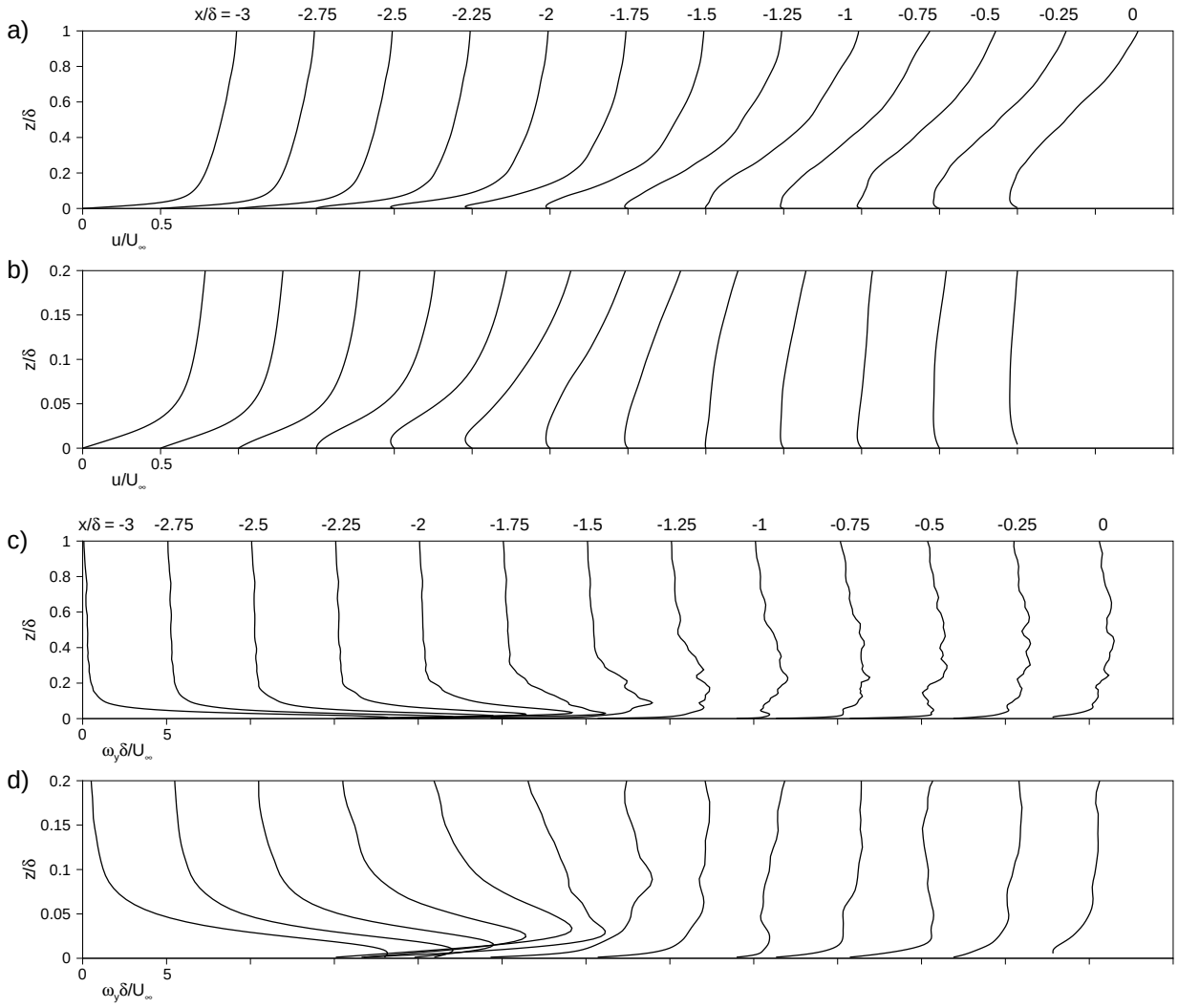

Figure 13. Same as figure 10, except that the profiles correspond to the low-pass filtered flow field shown in figure 9(*d*).

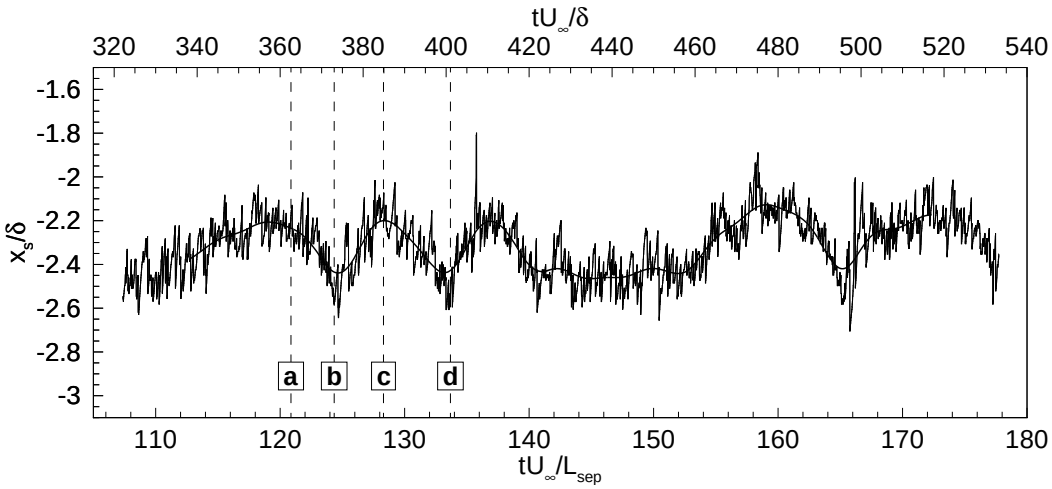

Figure 14. Time signal of separation location for detailed run 3. The low-pass filtered signal (with cutoff Strouhal number 0.22) is also shown.

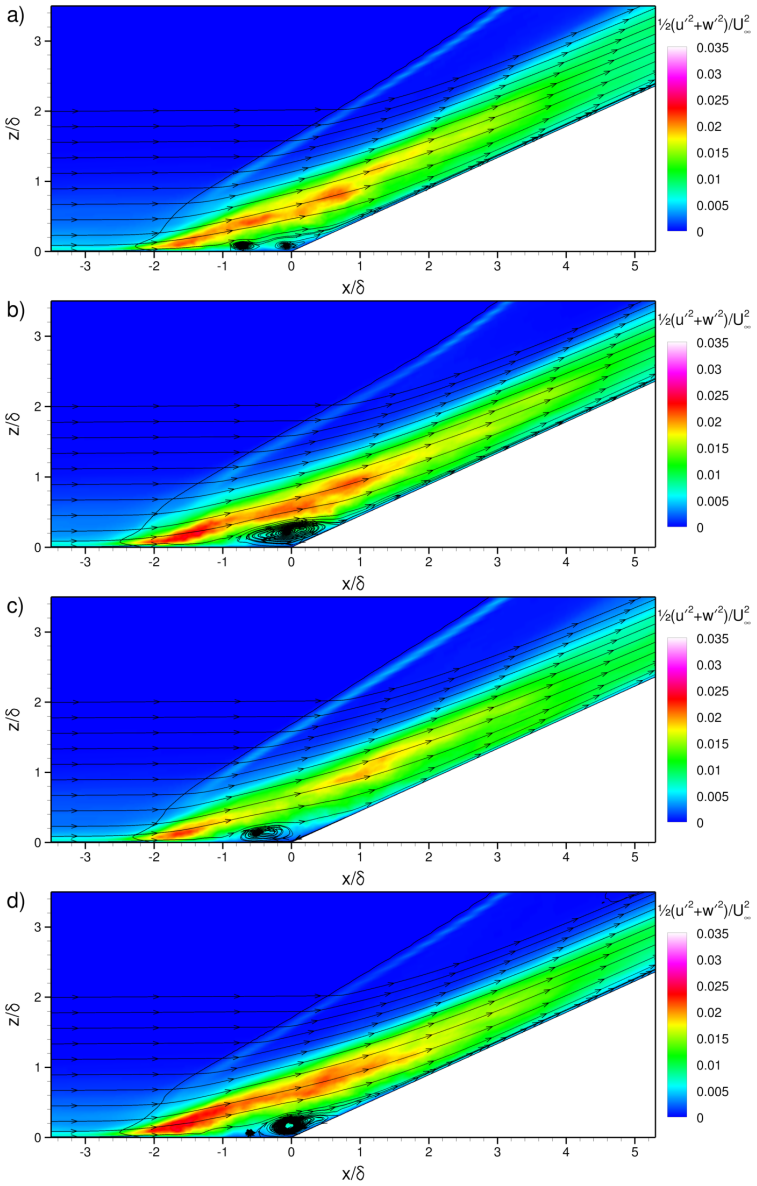

Figure 15. Instantaneous snapshots of low-pass filtered flow field.